SCIPEDIA

Studies of Shape Memory Graphene Nanostructures via Integration of Physics-based Modelling and Machine Learning

Carlos León, Roderick Melnik

INFORMATION

Keywords:
combining physiscs-based and machine learning approaches
complex systems
graphene nanostructures with shape memory effects
many-body tensor representation
DFT calculations
advanced scientific problems

DOI: 10.23967/coupled.2021.053

Published: 12/07/2021

IX International Conference on Computational Methods for Coupled Problems in Science and Engineering
COUPLED PROBLEMS 2021
E. Oñate, M. Papadrakakis and B. Schrefler (Eds)

STUDIES OF SHAPE MEMORY GRAPHENE NANOSTRUCTURES VIA INTEGRATION OF PHYSICS-BASED MODELLING AND MACHINE LEARNING

CARLOS LEÓN*, RODERICK MELNIK*†

*M3AI Laboratory, MS2Discovery Interdisciplinary Research Institute
Wilfrid Laurier University, Waterloo, ON, Canada N2L 3C5
e-mail: cleonchinchay@wlu.ca

†Basque Center for Applied Mathematics (BCAM)
E-48009, Bilbao, Spain
e-mail: rmelnik@wlu.ca

Key words: Physics-based Models, Machine Learning, Graphene Nanostructures with Shape Memory Effects, DFT, MBTR, SOAP

Abstract. In this contribution, we study the properties of new promising graphene-based materials with shape memory effects. While traditional shape memory alloys have been extensively studied, it is a challenge to preserve shape memory properties at the nanoscale. As a result, new materials have been explored, among which graphene oxide (GO) crystals with ordered epoxy groups where a recoverable strain of 14.5% has already been reported. We use such nanoscale GO structures as a benchmark example for our studies here. MBTR and SOAP representations are employed in a general-purpose ML model to analyze the effect of long-range interactions in GO. Finally, a physics-based ML model allows us to build interatomic potentials for 2D and 1D systems. The model predicts quantum mechanical effects due to the electronic confinement in narrow nanoribbons and shows the evolution of the local minimal energies associated with two-phase states.

1 INTRODUCTION

The interest in graphene and its derivatives has increased due to its novel properties. We particularly mention here a unique material based on a simple monomolecular layer of graphite with oxygen-containing functionalities, graphene oxide (GO). For this latter material, such interest is due to its cheaper and easy production compared to graphene [1], as well as because it can show an enhance-

ment of the desired properties depending on the functional groups attached to the system. The presence of oxygen-based functional groups in GO makes the system fluorescent due to the opening of the optical bandgap, and can be used for biological imaging [2], hydrogen storage [3, 4], water purification [5, 6], among other applications. GO is easy to deposit on a variety of substrates allowing its application in sensors and flexible electronics [7]. Due to its high surface area, it can be used for supercapacitor electrodes [8]. The content of oxygen epoxide groups modifies the electronic and optical properties of GO, and it can be tuned by applying laser energy doses [9]. GO can be synthesized by several methods, including bottom-up techniques, CVD, Hummer oxidation, and exfoliation of graphite [10]. GO can be mixed with different polymers to enhance its physical and chemical properties. It also systematically exhibits shape changes when incorporated with shape memory polymers (SMPs). Graphene nanocomposites with SMPs are fabricated in the form of films, foams, and stretchable networks [11], and can be employed as shape memory actuators due to their high electric conductivity, and oscillators when integrated with magnetic fields. The higher strain shown by GO can reinforce the shape memory effect when incorporated in polymers [12].

It is well known now that GO by itself, without the presence of a matrix, can also exhibit shape memory effects. It has been reported that a GO with highly ordered oxygen epoxide groups can experience recoverable strain rates up to 14%, paving the way for such applications as shape memory devices at the nanoscale dimensions [13, 14], resonators, artificial muscles, and molecular robots [15]. The GO sheet presents stable phases at two different lattice constants, separated by $\sim 100\,\text{meV}$ in the energy vs lattice constant space. It is the rearrangement of the electronic distribution at the carbon-oxygen-carbon edge that is responsible for the presence of these stable phases. The shape of the structure is characterized by a bend at the oxygen atoms row due to the different hybridizations between the carbon and oxygen atoms (sp2 for carbon, and sp3 for oxygen). After a force is applied to stretch the system, it can return to the original shape by the application of an electric field [13]. DFT calculations were performed for this discovery.

In this work, we use machine learning (ML) to study GO nanostructures to reduce the computational cost involved in the estimation of the two stable phases. Our goal here is twofold: to get a better insight into the characteristics behind the formation of the phases in a GO sheet, and to predict the response of GO nanoribbons.

2 METHODS

We focus our study on the C_8O structure defined in [13], with unit cell depicted in Fig.1. The system has periodicity along the X and Z directions, and thus defines a 2D sheet. The oxygen epoxy groups are ordered in rows and define

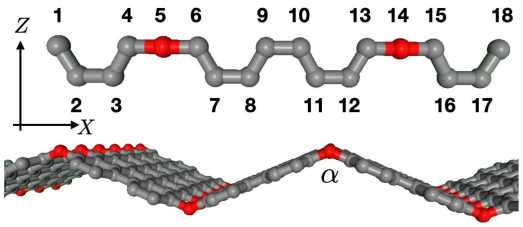

Figure 1: **Top**: Unit cell of the GO structure before structural optimization with lattice constant a_{lat} as the cell's length in the X-direction. **Bottom**: Side view of the relaxed GO structure. Gray (red) balls represent carbon (oxygen) atoms.

graphene stripes of zigzag interfaces. Fig.1 also shows the optimized structure using DFT calculations. The optimized structure is bent at the carbon-oxygen-carbon row, with angle α, and defines zigzag interfaces with the oxygen row of atoms. According to [13], the GO sheet posses two phases around $\alpha = 104°$ and 133° [13, 14], corresponding to lattice constants of $a_{\text{lat}} \sim 16\,\text{Å}$ and 18.5 Å. The two phases are separated by an energy of $\sim 100\,\text{meV}$. DFT calculations have been used in our study to validate results and compare them with those available in the literature. Specifically, we perform spin-polarized DFT calculations to relax the atomic positions at several fixed lattice constants. All of our DFT calculations were performed using the Quantum Espresso simulation package [16], using plane-wave basis sets and ultrasoft pseudopotentials [17], while employing the gradient approximation with the PBE exchange-correlation functional [18]. Our tests of convergence showed optimal values for a wavefunction energy cutoff of 60 Ry and a $4\times1\times4$ Monkhorst-Pack k-point grid (periodicity along the X- and Z- directions). Here we used an interlayer separation of 18 Å to ensure a minimum distance of ~ 12 Å between atoms, even with a bent structure for the range of lattice constant values considered (from $a_{\text{lat}} = 14$ Å to $a_{\text{lat}} = 19$ Å).

2.1 Moment tensor potentials for GO

After the validation, we have employed ML approaches that can mimic the DFT results and allows us to predict the behavior of nanoribbons with very big super unit cells, instead of the 2D system with the unit cell shown in Fig.1. We use a physics-based ML model designed for materials, coded in the MLIP package [19] to build an interatomic potential for the GO system.

The MLIP code is based on moment tensor potentials (MTP) [19, 20]. In this machine learning approach, the quantum mechanical energy of a structure (E_{QM}) is approximated as a sum of interatomic potentials (V) dependent on the atomic positions and species of the neighbor atoms (n)

$$E_{\mathrm{QM}} \approx \sum_i V(\mathrm{n}_i), \tag{1}$$

where n_i represents the neighborhood of the i-th atom, given by a collection of atomic position and species of each neighbor atom. V is expressed as an expansion of polynomials

$$V(\mathrm{n}_i) = \sum_{i=1}^{N} c_\alpha B_\alpha(\mathrm{n}_i), \tag{2}$$

where the expansion in the polynomial B_α and its construction ensures V to be invariant to structure's rotation and permutations of the same species elements. B_α is built in terms of the moment tensor potentials $M_{\mu,v}$ defined as

$$M_{\mu,v}(\mathrm{n}_i) = \sum_j |r_i|^{2\mu} r_i^{\otimes v}, \tag{3}$$

where $r_i^{\otimes v}$ indicates the v-times the kronecker product of r_i.

The model is trained by finding the coefficients c_α that best fit not only the quantum mechanical energy of the system in (1), but also the forces on each atom (derivative of (1) with respect to atomic positions), and stress values (proportional to the derivative of (1) with respect to lattice constants), values that were found in DFT results.

The forces and stress values were used to relax the atomic positions. In the relaxation process, the different configurations generated are graded according to geometric considerations. If a configuration is found to be an extrapolation from the training set and its grade is higher than a threshold grade value ("active learning"), a static DFT calculation is required on the new configuration to obtain the energy, forces, and stress.

2.2 Random forest regression for GO

For comparison purposes, we have also used another ML model, a random forest regressor due to its capabilities to handle high-dimensional data. Its implementation has been based on the Scikit-Learn ML python library [21]. For our case, features and targets are given by the atomic positions and their DFT energies, respectively. However, atomic positions need to be translated to a representation that is invariant to translation, rotation, inverse, and same-species atom permutation operations. The conversion from atomic environments into ML readable arrays is done by descriptors. Specifically, we use two implemented descriptors from the DScribe python package [22] that can handle the periodic nature of the GO sheet: the many-body tensor representation and the smooth overlap of atomic positions representation.

2.2.1 Many-body tensor representation (MBTR)

In the MBTR [23], chains of k-atoms are taken and a scalar is calculated according to their relative positions. For k=2, we assign the inverse of the distance between atoms as the scalar to represent a chain of 2 atoms. For k=3, the angle between a central atom and its two neighbors in a 3-body chain is taken as the scalar. We use an exponential weighting function with a cut-off radius of 14 Å (scale = 0.5, cutoff = 0.001) to remove contributions from far chains.

2.2.2 Smooth overlap of atomic positions (SOAP)

In the SOAP representation, the local density at one atomic site is the sum of the Gaussian functions centered at each of its atomic neighbors,

$$\rho(r) = \sum_i \exp\left(-\frac{(r_i - r)^2}{2\sigma^2}\right), \tag{4}$$

and the SOAP matrix elements are defined by the power spectrum

$$p_{Z_1 Z_2 n n' l}(r) \propto \sum_m c^*_{Z_1 nlm}(r) c_{Z_2 n' lm}(r), \tag{5}$$

where c_{Znlm} is the projection of the Gaussian function onto a radial basis function of degree n and the spherical harmonic of degree n and order m [22].

2.3 ML for GO wide nanoribbons

Finally, we extend the study to armchair GO nanoribbons (AGONRs) using a ML interatomic potential. To increase the accuracy in the prediction of the ML model, we use structures with relaxed atomic positions obtained from DFT calculations, at different lattice constants for both, a 2D system and an AGONR of 3 armchair lines, denoted as 3-AGONR. MTP can learn from the atomic environments of each structure, and we use the generated MTP potential as an interpolation tool to estimate the energy vs lattice structure evolution for different nanoribbon widths. This approach will let us study the effect of confinement on the shape memory behavior of a GO sheet, and the evolution of the two phases at finite nanoribbons widths.

3 RESULTS AND DISCUSSION

DFT validation results are shown in Fig.2(left). The 2D system exhibits a stable phase at ~ 18.5 Å and a metastable phase at ~ 15.5 Å, separated by an energy barrier of 60 meV. Fig.2(left) also contains information about the zigzag edge magnetization, i.e., the magnetization for the first-neighbor carbon atoms

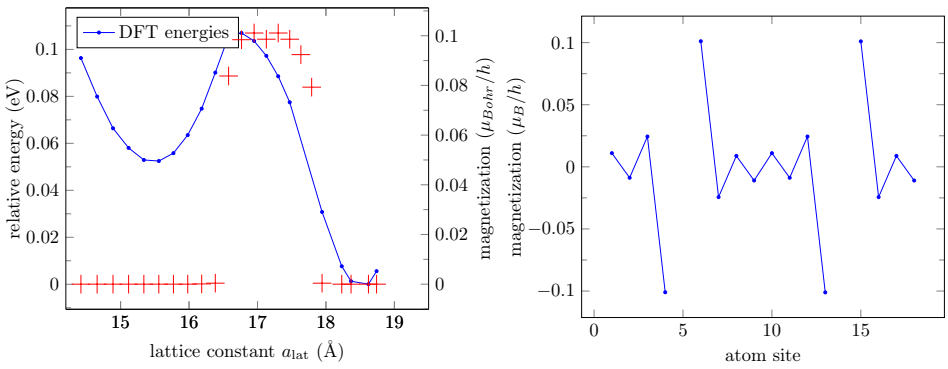

Figure 2: **Left**: DFT vs lattice constant in blue. Red marks indicate the zigzag edge magnetization around the oxygen atoms. **Right**: Magnetization for each atom site as defined in Fig.1, for lattice constant $a_{\text{lat}} = 17\,\text{Å}$

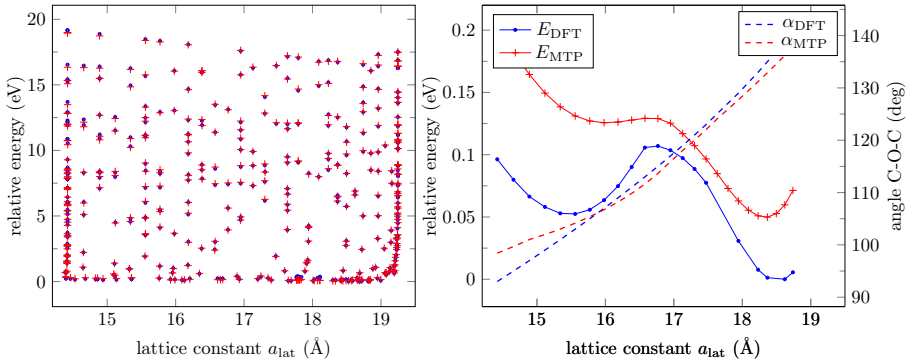

Figure 3: **Left**: Relaxed structures using DFT (blue) and MTP (red). The plot also contains the evolution of the angle C-O-C at the highly ordered epoxy groups. **Right**: Same DFT relaxed structures shown at the left plot (in blue) vs the energy prediction according to MTP (red)

around the oxygen atom, and distribution of the magnetization through the unit cell. Magnetization is zero for both phases, and reaches a maximum at the energy barrier around $a_{\text{lat}} = 17\,\text{Å}$. The row of oxygen atoms behaves as quantum wells, effectively isolating the zigzag stripes. However, this scenario might change by the application of an external electric field. It has been shown that the application of a critical electric field intensity, parallel to the plane of the nanoribbon, can turn off the metallic nature of electrons in one edge [24]. In the GO case, the metallic nature of electrons at one of the minima in Fig.2 might turn off for the right electric field intensity, and as a consequence, a rearrangement in the minima positions. This insight agrees with the results found in [13] when the applied electric field is perpendicular to the system. Since the system is bent at the oxygen positions, a parallel electric field can be decomposed from the original field direction. Note also that the authors of [13] show a critical electric field value

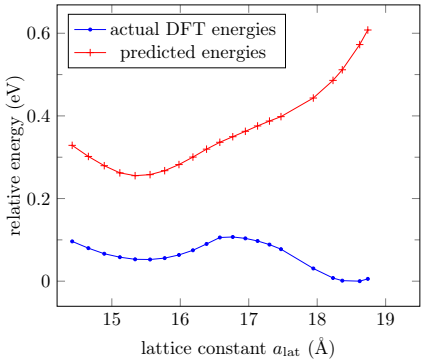

Figure 4: DFT (blue) vs predicted energy values using MTP (red) for optimized structures of different lattice constants

in which the system is no longer at the minimal energy, but evolutes into an intermediate metastable phase. Importantly, the magnetization around the zigzag interfaces might affect ML models that rely on the approximation shown in (1). To explore the magnetization effects, we can compare MTP with a general-purpose ML model predictions.

3.1 GO relaxation via MTP and DFT

For the ML model based on MTP, we have generated 300 structures, with oxygen atoms at different positions over a flat graphene sheet, and static DFT calculations were performed and the results were fed into MTP for training. In fact, an infinite number of possibilities can be proposed, but we let MTP choose representative structures from the relaxation trajectories of the initial training set. Through several iterations of relaxing, training, and active learning, convergence was achieved. During the active learning process, 399 representative structures were used to train the interatomic potential. These structures span over a range of 20 eV as shown in Fig.3(left). The error on the prediction was estimated to be a maximum of 0.30 eV, or 1.5%. Once the interatomic potential is built, it can be used to relax atomic positions. Fig.3(right) shows energy evolution for different lattice constants after relaxing the atomic positions either, by DFT or MTP. The MTP curve is shifted no more than 0.1 eV over the DFT results. MTP is not only able to predict the two phases, but also the energy barrier separation of the phases, $\sim$ 100 meV, which is approximately of the same order as the DFT results. The difference between MTP and DFT energies seems to be relatively high due to the low energy level window. To further increase the accuracy of the prediction, we can redo the fitting by taking only DFT results from the structures located in a narrow window width of some meV at the bottom of Fig.3(left), disregarding the energetic structures. After the iterative process of relaxation, active learning, and fitting achieves a convergence, we would have a trained interatomic potential

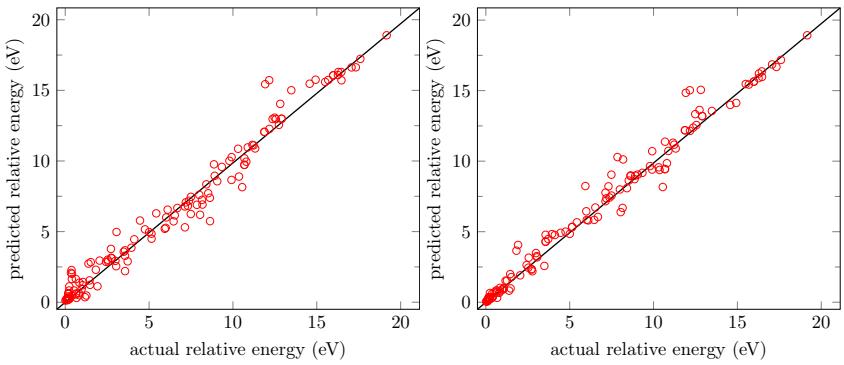

Figure 5: Performance of the fitting model vs the ideal performance (black line) $R^2 = 0.972$ for two-body representation (**right**), and $R^2 = 0.978$ for up to three-body representation (**left**)

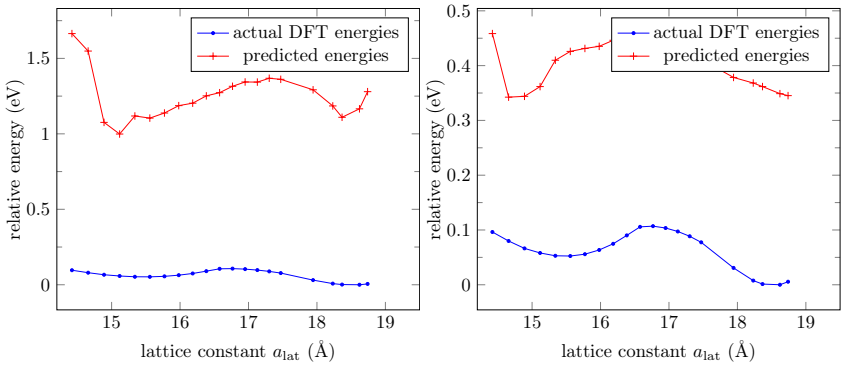

Figure 6: DFT vs predicted energy values for two-body representation (**right**), and for up to three-body representation (**left**)

which is more accurate, but only valid for the small window of energies considered.

Fig.4 shows the energies for the relaxed structures using DFT, and the MTP energy prediction of such structures. The plot does not show the same prediction performance compared to the relaxation performance (Fig.3). The reason might be attributed to long-range interactions in the GO system. MTP approximates the quantum mechanical energy of the system to a sum of local energies (Eq.1), and as stated in [20], the assumption may not be valid for all systems with long-range interactions. In the case of GO, long-range interactions can be originated from the polarized carbon atoms around the oxygen atoms as shown in Fig.2. In the following, we analyze the effect of the carbon-oxygen-carbon interactions on the total energy.

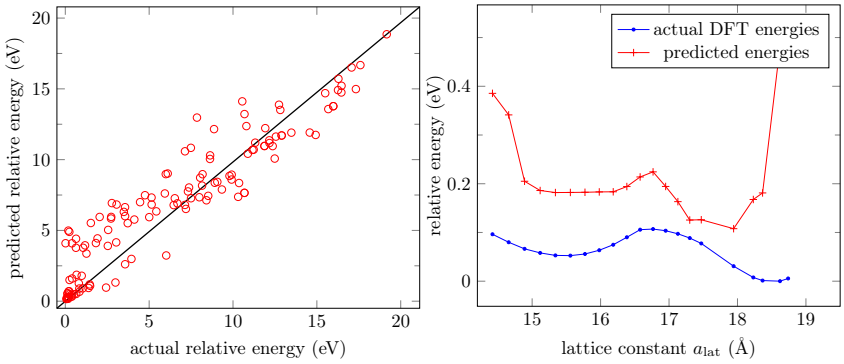

Figure 7: Performance of the fitting model vs the ideal performance (black line) $R^2 = 0.86$ for the SOAP representation (**right**), and DFT vs predicted energy values (**left**)

3.2 MBTR and SOAP representations for GO

We used the random forest regressor with two descriptors, MBTR and SOAP. Figures 5 and 6 show prediction performance and predicted energies for DFT relaxed structures, respectively. In the two-body representation, the features are calculated from the collection of the inverse of the distance for groups of two atoms. This representation can capture the two phases minima, but with a shifted energy of 1eV. The prediction improves if we use the three-body representation. The two phases minima disappear if we disregard interactions between atoms with distances greater than 3 Å.

To build the SOAP matrix representation, we take the contribution of all atoms, with a cut-off radius of 14 Å, on 4, 5, 6, 13, 14, and 15 sites only (oxygen and first-neighbor carbon atoms shown at Fig.1). An average on the mentioned sites over the matrix elements (see Eq.5) is performed to build the array of features. Fig.7 shows the performance prediction where it is seen that the two-phase minima get closer to the DFT curve when compared to the MBTR representation. Therefore, the main contribution to the total energy is due to the long-range interactions between the oxygen and carbon atoms at the epoxy groups with the rest of the atoms. The two minima in Fig.7 disappear if we consider instead an average over all atoms in the unit cell.

3.3 GO nanoribbon critical width

Even though the issues shown are related to long-range interactions, MTP can still be used to give an estimation of the total energy according to Eq.1 for different unit cells not contained in the training dataset. In contrast, without additional training, the random forest regression model would not be able to scale to correct energies even if the number of atoms increases. Therefore, we choose MTP to analyze the evolution of the stable phases in GO nanoribbons with different widths.

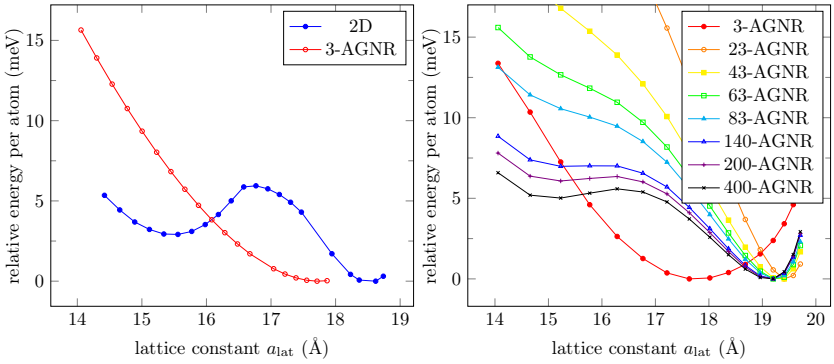

Figure 8: **Left**: DFT energy/atom of the relaxed GO sheet (blue) and a 3-AGONR (red) for different lattice constant values. **Right**: MTP energy prediction of n-AGONR for $n = 3, 23, 43, ..., 400$ armchair lines

Also, we choose MTP since wider nanoribbons with hundreds of atoms would be computationally expensive if only DFT calculations were used.

As mentioned in Section 2, to train the interatomic potential, we use DFT relaxed structures for both, a 2D system and a 3-AGONR. Fig.8(left) shows the curve of the total energy per atom relative to its minimum for the 2D GO system, and for an armchair GO nanoribbon with only 3 armchair lines (3-AGONR), and 26 atoms per unit cell. Fig.8(right) shows MTP energy predictions for different nanoribbon sizes. The stable phase is rapidly formed when increasing the nanoribbon width, while the metastable phase (at $a_{lat} \sim 15\,\text{Å}$) is formed at a slow rate. Therefore, the metastable phase is associated with the formation of new states due to the oxygen-oxygen interactions in the same row that strengthen as the width increases (the 3-AGONR has no oxygen-oxygen interactions). The metastable phase seems to be present at approximately 140 armchair lines, or at a critical width of $\sim 19\,\text{nm}$, although two minima are obtained at 400 armchair lines, or $\sim 50\,\text{nm}$. This critical value seems reasonable when compared to the critical size of 60 nm found for FePd nanostructures [25]. Here we have used a different approach on a different system to find a critical width in which the effect of confinement suppresses the shape memory behavior in GO nanoribbons.

4 CONCLUSIONS

- In this contribution, a physics-based ML model (MTP) has been developed to relax GO structures and to reproduce the two-phase minima in the energy vs lattice constant space, already obtained by DFT results.

- It has been demonstrated that the interatomic potential generated can be used to study nanoribbons with similar atomic environments found in the GO sheet.

- Moreover, we have found that the ML interatomic potential predicts a critical nanoribbon width of $\sim 50\,\text{Å}$, in which the two phases of the shape memory material are suppressed.

- Finally, MBTR and SOAP descriptors in a random forest regression have manifested the long-range effect of the magnetization around the oxygen-based epoxy groups.

REFERENCES

[1] Ranjan, P. et al. A low-cost non-explosive synthesis of graphene oxide for scalable applications. *Sci. Rep.* (2018) 8:12007.

[2] Zheng, P. and Wu, N. Fluorescence and sensing applications of graphene oxide and graphene quantum dots: A review. *Chem. Asian J.* (2017) 12:2343–2353.

[3] Jain, V. and Kandasubramanian, B. Functionalized graphene materials for hydrogen storage. *J. Mater. Sci.* (2020) 55:1865–1903.

[4] Samad, A. et al. Structure stability and high li storage capacity of the unzipped graphene oxide monolayer. *Appl. Surf. Sci.* (2019) 475:151–157.

[5] Alnoor, O. et al. Graphene oxide-based membranes for water purification applications: Effect of plasma treatment on the adhesion and stability of the synthesized membranes. *Membranes* (2020) 10(10), 292.

[6] Zhang, Y. et al. The preparation and study of ethylene glycol-modified graphene oxide membranes for water purification. *Polymers* (2019) 11(2), 188.

[7] Lin, X. et al. Excellent optoelectrical properties of graphene oxide thin films deposited on a flexible substrate by langmuir–blodgett assembly. *J. Mater. Chem. C* (2013) 1:6869–6877.

[8] Tian, J. et al. Novel preparation of hydrophilic graphene/graphene oxide nanosheets for supercapacitor electrode. *Appl. Surf. Sci.* (2019) 496:143696.

[9] Zheng, X. et al. In situ third-order non-linear responses during laser reduction of graphene oxide thin films towards on-chip non-linear photonic devices. *Adv. Mater.* (2014) 26:2699–2703.

[10] Dideikin, A. and Vul', A. Graphene oxide and derivatives: The place in graphene family. *Front. Phys.* (2019) 6:149.

[11] Wang, J. et al. Shape memory graphene and cutting-edge achievements. *APL Mater.* (2020) 8:050903.

[12] Zhang, X. et al. How graphene oxide affects shape memory properties and strength of poly(l-lactide-co-ϵ-aprolactone)). *J Intell Mater Syst Struct* (2020) 31:2152–2164.

[13] Chang, Z. et al. Two-dimensional shape memory graphene oxide. *Nat. Commun.* (2016) 7:11972.

[14] Chang, Z. et al. Two-way actuation of graphene oxide arising from quantum mechanical effects. *Appl. Phys. Lett.* (2016) 109:143902.

[15] Liu, J. and Hughes, J. Electromechanical actuation of pristine graphene and graphene oxide: origin, optimization, and comparison. arXiv:1903.02729 (2019).

[16] Giannozzi, P. et al. Quantum espresso: a modular and open-source software project for quantum simulations of materials. *J. Condens. Matter Phys.* (2009) 21:395502.

[17] Vanderbilt, D. Soft self-consistent pseudopotentials in a generalized eigenvalue formalism. *Phys. Rev. B* (1990) 41:7892–7895.

[18] Perdew, J. et al. Generalized gradient approximation made simple. *Phys. Rev. Lett.* (1996) 77:3865–3868.

[19] Novikov, I. et al. The mlip package: Moment tensor potentials with mpi and active learning. arXiv:2007.08555 (2020).

[20] Shapeev, A. Moment tensor potentials: A class of systematically improvable interatomic potentials. *Multiscale Modeling Sim.* (2016) 14:1153–1173.

[21] Pedregosa, F. et al. Scikit-learn: Machine learning in Python. *J Mach Learn Res* (2011) 12:2825–2830.

[22] Himanen, L. et al. Dscribe: Library of descriptors for machine learning in materials science. *Comput. Phys. Commun.* (2020) 247:106949.

[23] Huo, H. and Rupp, M. Unified representation of molecules and crystals for machine learning. arXiv:1704.06439 (2018).

[24] Son, Y. et al. Half-metallic graphene nanoribbons. *Nature* (2006) 444:347–349.

[25] Dhote, R. et al. Dynamic thermo-mechanical coupling and size effects in finite shape memory alloy nanostructures. *Comput. Mater. Sci.* (2012) 63:105–117.